1
2

Transhydrogenase and growth substrate influence lipid hydrogen isotope ratios in *Desulfovibrio alaskensis* G20

3

4 **William D. Leavitt[1*], Theodore M. Flynn[2], Melanie K. Suess[1], Alexander S.**
5 **Bradley[1,3*]**

6 1. Department of Earth and Planetary Sciences, Washington University in St. Louis, Saint Louis, MO, USA

7 2. Biosciences Division, Argonne National Laboratory, Argonne, IL, USA

8 3. Division of Biology and Biomedical Sciences, Washington University in St. Louis, Saint Louis MO,
9 USA

10 ***Correspondence**: William D. Leavitt, Department of Earth and Planetary Sciences, Washington
11 University in St. Louis, 1 Brookings Drive, Saint Louis, MO 63130 USA
12 wleavitt@eps.wustl.edu

13 ***Correspondence**: Alexander S. Bradley, Department of Earth and Planetary Sciences, Washington
14 University in St. Louis, 1 Brookings Drive, Saint Louis, MO 63130 USA
15 abradley@eps.wustl.edu

16 **Keywords**: compound specific hydrogen isotopes, transhydrogenase, lipid biomarkers,
17 dissimilatory sulfate reduction.

18

19 **Abstract**

20 Microbial fatty acids preserve metabolic and environmental information in their hydrogen
21 isotope ratios (^{2}H/^{1}H). This ratio is influenced by parameters that include the ^{2}H/^{1}H of
22 water in the microbial growth environment, and biosynthetic fractionations between
23 water and lipid. In some microbes, this biosynthetic fractionation has been shown to vary
24 systematically with central energy metabolism, and controls on fatty acid ^{2}H/^{1}H may be
25 linked to the intracellular production of NADPH. We examined the apparent fractionation
26 between media water and the fatty acids produced by *Desulfovibrio alaskensis* G20.
27 Growth was in batch culture with malate as an electron donor for sulfate respiration, and
28 with pyruvate and fumarate as substrates for fermentation and for sulfate respiration. A
29 larger fractionation was observed as a consequence of respiratory or fermentative growth
30 on pyruvate than growth on fumarate or malate. This difference correlates with opposite
31 apparent flows of electrons through the electron bifurcating/confurcating
32 transhydrogenase NfnAB. When grown on malate or fumarate, mutant strains of *D.
33 alaskensis* G20 containing transposon disruptions in a copy of *nfnAB* show different
34 fractionations than the wild type strain. This phenotype is muted during fermentative
35 growth on pyruvate, and it is absent when pyruvate is a substrate for sulfate reduction.
36 All strains and conditions produced similar fatty acid profiles, and the ^{2}H/^{1}H of individual
37 lipids changed in concert with the mass-weighted average. Unsaturated fatty acids were
38 generally depleted in ^{2}H relative to their saturated homologues, and anteiso- branched
39 fatty acids were generally depleted in ^{2}H relative to straight-chain fatty acids.
40 Fractionation correlated with growth rate, a pattern that has also been observed in the
41 fractionation of sulfur isotopes during dissimilatory sulfate reduction by sulfate reducing
42 bacteria.

43
44

1   Introduction

The structures and isotopic compositions of lipids preserve information about organisms that can be archived in sediments and rocks over geological time scales. Understanding how to interpret this information is a central task of organic geochemistry. Lipid structures can be affiliated to particular groups of organisms (Pearson, 2014), and ratios of carbon isotopes in lipids record information about carbon sources and assimilation pathways (Hayes, 2001; Smith and Epstein, 1970) The ratio of hydrogen isotopes (deuterium/protium = $^2H/^1H$), in lipids derived from environmental samples has been observed to relate to the $^2H/^1H$ of environmental water (Hayes, 2001; Sauer et al., 2001). More recently, it was shown in a range of aerobic microorganisms that the fractionation of hydrogen isotopes between media water and lipids varied with changes in growth substrate (Zhang et al., 2009). Experiments with anaerobes have shown less systematic changes in lipid $^2H/^1H$ as a function of energy metabolism, although strong differences have been observed in lipid $^2H/^1H$ of organisms in pure culture versus co-cultures with another organism (Dawson et al., 2015; Osburn, 2013; Osburn et al., 2016).

Observations that lipid $^2H/^1H$ varies as a function of growth substrate in many microorganisms raises the question of what specific metabolic mechanisms are responsible. Zhang et al. (2009) considered several explanations, and through a process of elimination, deduced that observed differences in lipid $^2H/^1H$ must be a consequence of differences in the NAD(P)H that serves as a hydride donor during lipid biosynthesis. These authors pointed out that cells have multiple pathways for producing NAD(P)H, and that the relative importance of each of these mechanisms varies with differences in growth conditions. One mechanism considered was alteration of the $^2H/^1H$ ratio of the transferrable hydride in NAD(P)H by transhydrogenase enzymes. This suggestion stems from two key observations. First, up to half of the hydrogen atoms in microbial lipids are derived directly from NADPH during biosynthesis (Jackson, 2003; Saito et al., 1980). Second, in vitro observations of the hydrogen isotope fractionation imparted by transhydrogenase suggest that it is very large (> 800‰) (Bizouarn et al., 1995; Jackson et al., 1999; Venning et al., 1998).

In this study, we vary substrates and use mutant strains to investigate the importance of a transhydrogenase (NADH-dependent reduced ferredoxin:NADP oxidoreductase; NfnAB) on the lipid $^2H/^1H$ ratios in an anaerobic microorganism, *Desulfovibrio alaskensis* G20. Recent work has suggested that NfnAB plays an important role in energy conservation in this microbe (Price et al., 2014). The role of NfnAB varies as a function of the growth substrate. During growth on malate, for example, NfnAB is predicted to catalyze an electron bifurcation reaction (Buckel and Thauer, 2013) in which NADPH reduces ferredoxin and NAD^+ to produce NADH (Figure 1). Conversely, during growth on pyruvate, NfnAB is predicted to catalyze electron confurcation and the production of NADPH from NADH, $NADP^+$, and reduced ferredoxin. The importance of this transhydrogenase to anaerobic energy metabolism may be critical to understanding lipid H-isotope signatures. Since the transhydrogenase reaction catalyzed by NfnAB is predicted to occur in opposite directions during growth on pyruvate versus that on malate, the lipids produced under each condition should have different $^2H/^1H$ ratios if NfnAB is

91   indeed a significant source of isotope fractionation for intracellular hydrogen.
92   Furthermore, the role of NfnAB in hydrogen isotope fractionation can be further explored
93   using mutant strains of *D. alaskensis* G20 in which the NfnAB-2 loci have been
94   disrupted.
95
96   **2   Material and Methods**
97   **2.1   Strains, growth media, culture conditions and biomass sampling**
98
99   Wild type *Desulfovibrio alaskensis* G20 was obtained along with two mutant strains from
100 the library collection at Lawrence Berkeley National Laboratory. Each mutant contains a
101 Tn5 transposon insertion into a gene of interest. These insertions (Kuehl et al., 2014)
102 were into the genes *nfnA*-2 at locus Dde_1250 (strain JK00256) and *nfn*B-2 at locus
103 Dde_1251 (JK01775). Hereafter, these strains are referred to as the *nfnA*-2 and *nfnB*-2
104 mutants. These loci encode the subunits for one of two paralogs of NfnAB in *D.*
105 *alaskensis* G20.
106
107 All strains were resuscitated from 10% glycerol freezer stocks stored at -80 °C.
108 Resuscitated strains were inoculated into serum bottles containing approximately 50 ml
109 of a rich lactate/sulfate medium containing yeast extract (MOY_LS) and incubated at
110 30 °C. After reaching stationary phase, strains were then serially transferred three times
111 in a defined lactate/sulfate (80 mM/40 mM) medium (MO_LS). Late-log phase cultures
112 of the third transfer were diluted 1 to 100 into duplicate bottles for each isotope
113 fractionation experiment. There were five experimental growth conditions, which
114 combined an electron donor and 40 mM sulfate (for sulfate respiration), or an electron
115 donor alone for fermentation. The five conditions were: pyruvate/sulfate respiration,
116 malate/sulfate respiration, fumarate/sulfate respiration, pyruvate fermentation, fumarate
117 fermentation.
118
119 The basal growth medium recipe (MO) was as follows: 8 mM magnesium chloride, 20
120 mM ammonium chloride, 0.6 mM calcium chloride, 6 mL/L trace elements solution (see
121 below), 0.12 mM of $FeCl_2$ (125mM)+EDTA (250 mM) stock solution, 30 mM Tris-HCl
122 (2M, pH 7.4 stock). Sodium thioglycolate (0.12 g/L) was added as a reductant following
123 initial degassing. MO medium containing yeast extract (MOY) is generated by adding
124 yeast extract (0.1% w/v) to MO medium from an anoxic sterile stock. Media were made
125 anaerobic by degassing with O_2-free N_2 that had been filtered through sterile 0.22 μm
126 syringe filters. Solutions were degassed for 2 hours per liter. The pH of the final medium
127 was adjusted to 7.2 using sterile and anoxic HCl or NaOH, autoclave-sterilized, and then
128 cooled under sterile O_2-free N_2. After cooling, phosphate solution was added to a final
129 concentration of 2 mM from a sterile, anoxic stock solution of K_2HPO_4+NaH_2PO_4.
130 Thauer's Vitamins were added from a 1000x stock (Rabus et al., 2015). The initial
131 concentration of sulfate was always 40 mM (except in fermentation experiments) and was
132 added directly to the medium from a sterile and anoxic stock solution of Na_2SO_4 solution.
133 Electron donors (sodium lactate, sodium pyruvate, malic acid, or sodium fumarate) were
134 prepared separately as 1M stocks in MilliQ water, adjusted to a pH of 7.2, and degassed
135 in a manner similar to the basal media. These anoxic stocks were then added to the basal
136 media using aseptic technique.

137
138 Growth rate was determined by monitoring changes in optical density (OD_{600}) over time
139 for each experiment. Replicate cultures were tracked through log-phase and into early
140 stationary phase, at which point they were harvested for biomass. Growth rates were
141 calculated using a modified logistic equation (Rabus et al., 2006) and averaged across the
142 apparent log-phase of growth. In experiments showing diauxic growth, we calculated a
143 weighted average growth rate, where weighting accounts for the amount of biomass
144 produced during each growth interval.

145
146 Duplicate 50mL cultures were harvested at the onset of early stationary phase by opening
147 the serum bottles, decanting the remainder of each serum bottle (> 40mL) into sterile
148 50mL conical tubes, and centrifuging at 5000 rpm at 5 °C for 30 minutes. Spent medium
149 was decanted into a fresh 50mL tube and frozen at -80 °C for later analysis of the isotopic
150 composition of water therein. The biomass pellet was frozen at -80 °C, transferred to a
151 pre-baked and weighed 4mL borosilicate glass vial, lyophilized, and weighed.

152
153 **2.2   Fatty acid extraction, identification, and quantitation**

154
155 Samples were simultaneously extracted and derivatized to fatty acid methyl ethers
156 (FAMEs) by adding a mixture of hexane, methanol and acetyl chloride to the lyophilized
157 cell pellet, followed by heating at 100 °C for 10 minutes, and extraction with hexane
158 (Rodriguez-Ruiz et al., 1998; Zhang et al., 2009). This procedure was also concurrently
159 performed on two isotope standards, myristic acid and phthalic acid, for which the δ^2H of
160 non-exchangeable hydrogen has been determined (Qi and Coplen, 2011). Each sample
161 was reacted with acid-activated copper shot to remove elemental sulfur, and then
162 concentrated under a stream of dry hydrocarbon-free nitrogen.

163
164 Individual FAMEs were analyzed using a HP 7890 gas chromatograph fitted with a
165 split/splitless injector operated in splitless mode, equipped with a J&W DB-5 fused silica
166 capillary column (30 m length, 0.25-mm inner diameter, and 0.25-μm film thickness) and
167 coupled to an Agilent 6973 mass selective detector. FAME identifications were based on
168 mass spectra and retention times and are reported in Table S1. Retention times were
169 converted to Kovats retention indices by comparison to a mix of n-alkanes, and compared
170 to the retention indices of published fatty acids (Dickschat et al., 2011; Taylor and
171 Parkes, 1983). Double bond locations were identified by converting unsaturated fatty
172 acids to their dimethyl disulfide adducts (Nichols et al., 1986). Abundances were
173 determined by peak area as calculated in Chemstation (Agilent Technologies, Santa
174 Clara, CA) relative to a known amount of co-injected methyl tetracosanoate (C24:0).

175
176 **2.3   Isotopic measurements and data handling**

177
178 Hydrogen-isotopic compositions of individual FAMEs were determined using a TraceGC
179 gas chromatograph fitted with a column identical to that on the Agilent GC, and coupled
180 to a Thermo Scientific Delta V Plus isotope-ratio-monitoring mass spectrometer via a
181 Thermo GC-Isolink pyrolysis interface at 1400 °C. Column temperature was initially
182 60 °C and was increased at a rate of 6 °C min^{-1} until reaching a final temperature of

183 320 °C. Hydrogen isotope ratios of individual lipids were determined relative to
184 coinjected methyl tetracosanoate (C24:0) of known isotopic composition, provided by Dr.
185 A. Schimmelmann (Indiana University). Instrumental precision was regularly monitored
186 by analyzing the δ^2H on external standard mixtures of FAMEs and of *n*-alkanes with
187 previously determined isotopic composition (V-SMOW), also purchased from Dr.
188 Schimmelmann (Indiana University). Over the measurement period the mean RMS error
189 on a mixture of 8 FAMEs was 5.5‰ (n = 286). Samples were discarded if they were not
190 bracketed by injections of FAMEs mixture with an RMS better than 7‰. H_3 factors were
191 determined daily and had a mean value of 2.98 ± 0.3 ppm/nA. All FAME isotopic
192 compositions were corrected by mass balance for the hydrogen present in the methyl
193 group, calculated from them myristic acid and phthalic acid isotopic standards. Samples
194 were reinjected (pseudoreplicates) three to six times, and errors were propagated
195 following established methods (Polissar and D'Andrea, 2014). Statistical analyses were
196 performed in either Prism (GraphPad Software, Inc., La Jolla, CA) or R (RCoreTeam,
197 2015).
198
199 All ^{2}H/^{1}H ratios are reported as δ^2H values relative to V-SMOW, and fractionations are
200 reported as apparent fractionations between media water and lipid by the equation: $^2\varepsilon_{\text{lipid-}}$
201 $_{\text{water}}$ = ($\alpha_{\text{lipid-water}}$ - 1), where α = [(δ ^{2}H$_{\text{lipid}}$ + 1)/(δ^2H$_{\text{water}}$ + 1)] and are reported in ‰. The
202 δ^2H$_{\text{water}}$ of growth media water was measured using a Picarro L2130-*i* cavity ring-down
203 spectrometer at Northwestern University.
204
205 **2.4   Comparative analysis of *nfnAB* sequences**
206
207 We constructed a gene tree of *nfnAB* sequences by retrieving data from two public
208 repositories of annotated genomes: the SEED (Overbeek et al., 2014) and IMG
209 (Markowitz et al., 2012). For this study, we restricted sequences to those also found in
210 the subsystem "NADH-dependent reduced ferredoxin:NADP+ oxidoreductase" in the
211 SEED (197 total sequences) and manually refined the list to sequences from known
212 sulfate reducers, methanogens, and other anaerobes. Sequences from organisms known to
213 contain *nfnAB* but not present in the SEED were added manually using a targeted amino
214 acid BLAST search of that organism's genome in the IMG database. This resulted in a
215 total of 105 *nfnAB* sequences closely related to that of *D. alaskensis* G20 using
216 established criteria (Marti-Renom et al., 2000; Rost, 1999), with > 40% amino acid
217 identity and BLASTP percent identities ranging from 45–77%. *D. alaskensis* G20 itself
218 has two copies of *nfnAB* that share 85% amino acid identity. A multiple sequence
219 alignment of the 105 putative *nfnAB* sequences was created using MUSCLE (Edgar,
220 2004) and checked manually using AliView (Larsson, 2014). Alignments in FASTA
221 format are available to download in the Supplementary Materials. Pairwise distances for
222 construction of a phylogenetic tree were calculated using the RAxML maximum
223 likelihood algorithm (Stamatakis, 2006) with the program raxmlGUI (Silvestro and
224 Michalak, 2012). The tree itself was generated using the Interactive Tree of Life software
225 (Letunic and Bork, 2011).
226
227 **3.   Results**
228 **3.1   Growth rates**

229
230   Growth experiments revealed distinct physiological and isotopic phenotypes among the
231   wild type and mutant strains of *D. alaskensis* G20. Growth rates are reported in Table 1
232   and growth curves are plotted in Figure 2.
233
234   Some growth conditions showed clear phenotypic differences between the *D. alaskensis*
235   G20 wild type and the two *nfnAB-2* mutants. Each strain was able to grow as a sulfate
236   reducer using malate as an electron donor, but the growth rate of the mutants was only
237   22% that of the wild type. Similarly, with fumarate as an electron donor coupled to
238   sulfate reduction, mutant growth rate was roughly 10% that of the wild type. A repression
239   in growth rate (22% of wild type) was also apparent when the strains were grown as
240   fumarate fermenters, in the absence of sulfate. Under all of these conditions, the final
241   optical density of the mutant cultures was less than that of the wild type (Figure 2). The
242   mutant strains exhibited diauxic growth under each of these growth conditions whereas
243   the wild type did not (Figure 2).
244
245   **3.2   Lipid profiles**
246
247   We quantified the abundance of fatty acid structures in each of the three strains under all
248   five experimental conditions (pyruvate/sulfate, malate/sulfate, fumarate/sulfate, fumarate
249   fermentation, or pyruvate fermentation). Fatty acids ranged in carbon number from 14 to
250   18, and both saturated and monounsaturated fatty acids were present. Branched-chain
251   fatty acids of the iso- and anteiso- series are present in all three strains under all five
252   experimental conditions. Branched fatty acids contained a total of 15 to 18 carbons, and
253   in some cases contained a double bound.
254
255   Differences in the lipid profiles of the mutant relative to the wild type were apparent only
256   under the three conditions in which the mutant showed a growth defect: malate/sulfate,
257   fumarate/sulfate, and fumarate fermentation (Figures 3b, 3c, 3d). During growth on
258   malate/sulfate, the *nfn*AB-2 mutant strains contain a higher proportion of anteiso-C17:0,
259   and a lower proportion of C16:0, C18:0, and iso-C15:0 fatty acids. A similar pattern is
260   seen in the mutants during growth on fumarate/sulfate and during fumarate fermentation,
261   although the C18 patterns are slightly different. Differences in the abundance of anteiso-
262   C17:0 fatty acid is most pronounced in these three growth conditions. In contrast, during
263   both respiratory and fermentative growth on pyruvate, the fatty acid profile of the wild
264   type and mutants were nearly identical (Figures 3a, 3e). Across all strains and conditions,
265   there is a weak inverse correlation between the proportion of branched fatty acids (Figure
266   S1a) or the ratio of anteiso- to iso- branched compounds (Figure S1b), in each case
267   relative to the mass weighted fractionation. Data used to generate these plots are
268   deposited in a permanent repository at Figshare: doi:10.6084/m9.figshare.2132731.
269
270   **3.3   Lipid ^{2}H/^{1}H fractionations**
271
272   We calculated $\delta^2 H_{total}$ as the weighted average of the $\delta^2 H_{lipid}$ of each individual fatty acid
273   pool produced in each strain. We then calculated a total apparent fractionation ($^2\varepsilon_{total}$) for
274   the fatty acid pool (Sessions and Hayes, 2005). The results are shown in Figure 4.

275   Apparent fractionations produced by the wild type strain were not discernable between
276   pyruvate/sulfate respiration ($^2\varepsilon_{total}$ = -171‰) and pyruvate fermentation ($^2\varepsilon_{total}$ = -168‰).
277   Similarly, both *nfn* mutants have $^2\varepsilon_{total}$ = -171‰ when grown by pyruvate/sulfate
278   respiration. However, *nfn* mutants that grew by fermenting pyruvate had $^2\varepsilon_{total}$ = -160‰
279   for the *nfnA*-2 mutant and $^2\varepsilon_{total}$ = -162‰ for the *nfnB*-2 mutant.

280

281   Differences in $^2\varepsilon_{total}$ were more pronounced in the other growth conditions. In comparison
282   to growth on pyruvate, the wild type strain showed less negative $^2\varepsilon_{total}$ as a consequence
283   of malate/sulfate growth ($^2\varepsilon_{total}$ = -143‰), fumarate/sulfate growth ($^2\varepsilon_{total}$ = -135‰), and
284   fumarate fermentation ($^2\varepsilon_{total}$ = -142‰). The *nfn* mutants showed even stronger isotopic
285   phenotypes. The *nfnA*-2 mutant had less negative $^2\varepsilon_{total}$ than the wild type during growth
286   on malate/sulfate ($^2\varepsilon_{total}$ = -82‰), fumarate/sulfate ($^2\varepsilon_{total}$ = -103‰), and fumarate ($^2\varepsilon_{total}$ =
287   -108‰). The magnitude of fractionation by the *nfnB*-2 mutant was consistently less than
288   that of both the wild type and the *nfnA*-2 mutant on malate/sulfate ($^2\varepsilon_{total}$ = -59‰),
289   fumarate/sulfate ($^2\varepsilon_{total}$ = -72‰), and fumarate ($^2\varepsilon_{total}$ = -72‰).

290

291   The δ^2H_{lipid} of individual lipids can help explain some of these patterns. Most lipids from
292   our cultures were depleted in deuterium by between -50‰ and -250‰ relative to the
293   water in the growth medium. Figures 5 summarize the results from each strain. The
294   various lipid structures produced by each strain had a wide range of $^2\varepsilon_{lipid}$, but isotopic
295   ordering among lipids was remarkably consistent. Figure 5 shows $^2\varepsilon_{lipid}$ values for the
296   most abundant lipids in each combination of strain and culture conditions. For all three
297   strains, across nearly every culture condition, the fatty acid with the largest $^2\varepsilon_{lipid}$ was
298   C16:1. The exceptions to this were produced by the pyruvate fermentation experiments,
299   in which the largest $^2\varepsilon_{lipid}$ observed was in anteiso-C17:1 in all three strains, and by
300   fumarate fermentation by the mutants, where the C16:1 was in too low abundance for δ^2H
301   measurements (Figure 5). Across all sulfate reduction experiments, fatty acids containing
302   a double bond were nearly always depleted relative to their saturated homologue. This
303   was true for both straight-chain and branched fatty acids. Differences in δ^2H were larger
304   between C16 and C16:1 than between C18 and C18:1, driven by the particularly strong
305   ^2H depletion in C16:1. This pattern was muted in the fermentation experiments. We also
306   found that saturated anteiso- branched fatty acids produced during sulfate reduction were
307   always depleted relative to straight-chain fatty acids. This pattern did not hold for
308   unsaturated anteiso- fatty acids or for lipids produced during fermentation. Saturated iso-
309   branched fatty acids had similar δ^2H as saturated straight-chain fatty acids. The lipid with
310   the least negative $^2\varepsilon_{lipid}$ was iso-C18:0 (Figure 5). When produced under certain sulfate
311   reducing conditions this lipid was enriched in ^2H relative to media water ($^2\varepsilon_{lipid}$ > 0‰).
312   Under fermentative conditions, this lipid was produced in insufficient abundance to
313   measure δ^2H_{lipid}.

314

315   The regular ordering of lipid δ^2H values suggests that the variations in $^2\varepsilon_{total}$ were mainly
316   a function of a systematic change in $^2\varepsilon$ from one condition to another rather than changes
317   in the relative proportion of individual lipids that are particularly enriched or depleted. In
318   Figure 5 the thick black line and circles show $^2\varepsilon_{total}$, highlighting the relationship between
319    $^2\varepsilon_{lipid}$ and $^2\varepsilon_{total}$ for each strain and culture condition. With few exceptions, a consistent
320   pattern emerged in the relative fractionation of each lipid relative to the weighted

321 average. Together, Figures 4 and 5 indicate the presence of significant differences
322 between the wildtype and mutants for growth on malate/sulfate, fumarate/sulfate or
323 fumarate fermentation, while little to no difference existed between strains grown on
324 pyruvate/sulfate or pyruvate fermentation.
325
326 We examined whether changes in the abundance of particular lipids were correlated with
327 each other, with growth rate, or with $^2\varepsilon_{total}$. A graphical display of Pearson correlation
328 indices for each variable pair is shown in Figure S3 This indicates that $^2\varepsilon_{total}$ is strongly
329 correlated with the relative abundance anteiso-C17:0 fatty acid, and negatively correlated
330 with C16 and C16:1 fatty acid. However, the relative abundance of each of these fatty
331 acids was strongly correlated (negatively, for anteiso-C17:0 fatty acid) with average
332 growth rate (μ). Growth rate emerged as a strong correlate of $^2\varepsilon_{total}$ (Figure 6).
333
334
335 **4.   Discussion**
336 **4.1   Hydrogen isotopes and intracellular electron flow**
337
338 This study aims at improving our understanding of the influence of intracellular
339 mechanisms that contribute to the $^2H/^1H$ ratios in lipids. Zhang et al. (2009) suggested
340 that mechanisms related to the purine dinucleotide coenzymes NAD(P)H are central to
341 determining δ^2H_{lipid}. In particular, that work suggested that H-isotopic fractionation by
342 transhydrogenase was one potential mechanism for changing the H-isotopic composition
343 of the transferable hydride on NAD(P)H. This is mainly due to the observations that
344 NADPH directly provides up to 50% of lipid hydrogen (Robins et al., 2003; Saito et al.,
345 1980; Schmidt et al., 2003), and predictions that δ^2H_{NADPH} and abundance may vary with
346 growth condition.
347
348 *Desulfovibrio* can produce NADPH via a number of mechanisms. Gram negative bacteria
349 synthesize $NADP^+$ from NAD^+ by ATP-requiring NAD-kinase, but can not convert
350 NADH to NADPH via this mechanism (Kawai and Murata, 2008). A number of
351 metabolic reactions produce NADPH by reducing $NADP^+$. Major mechanisms include
352 enzymes within the tricarboxylic acid cycle, the oxidative pentose phosphate pathway,
353 and mixed acid fermentation pathways. The relative importance of each of these
354 mechanisms varies by substrate, and potential differences δ^2H_{NADPH} produced by these
355 mechanisms has been invoked as a major reason for differences in δ^2H_{lipid} produced by
356 organisms grown on various substrates (Zhang et al., 2009). Transhydrogenases are
357 another mechanism for NADPH production. In addition to the Nfn family of
358 transhydrogenase found in aerobes (Wang et al., 2010), two other families of
359 transhydrogenases are common in aerobes: the proton-translocating transhydrogenase
360 PntAB, and the energy-independent transhydrogenase UdhA (Sauer et al., 2004). These
361 two enzymes have been discussed as a potential mechanism of influencing the δ^2H of
362 lipids (Dawson et al., 2015; Osburn et al., 2016; Zhang et al., 2009). Major mechanisms
363 of NADPH production are summarized by Spaans et al. (2015), and those mechanisms
364 relevant to *Desulfovibrio alaskensis* G20 are summarized in Table S2.
365

366   Previous work on hydrogen isotope fractionation in sulfate reducing bacteria (SRB)
367   includes studies of pure cultures of *Desulfobacterium autotrophicum* (Campbell et al.,
368   2009; Osburn, 2013), *Desulfobacter hydrogenophilus* and *Desulfovibrio alaskensis* G20
369   (Osburn, 2013) and of *Desulfococcus multivorans* in pure culture and in co-culture with a
370   methanogen (Dawson et al., 2015). Results contrast with those obtained from aerobes, in
371   which growth on different carbon sources results in a large range of $^2\varepsilon_{total}$ (Zhang et al.,
372   2009). *D. Autotrophicum* shows a smaller range in $^2\varepsilon_{total}$ (~45‰) during heterotrophic
373   growth on acetate, succinate, pyruvate, glucose, or formate, or autotrophic growth on
374   H_2/CO_2, yet there are large differences in the $^2\varepsilon_{lipid}$ of individual fatty acids (differences of
375   >100 ‰) (Campbell et al., 2009; Osburn, 2013). *D. hydrogenophilus* and *D. multivorans*
376   grown in pure cultures generate an ~80‰ range in $^2\varepsilon_{total}$ during heterotrophic growth;
377   though when *D. multivorans* was growing in co-culture with the methanogen
378   *Methanosarcina acetivorans* it produced a more muted range in $^2\varepsilon_{total}$ of ~36‰ (Dawson
379   et al., 2015; Osburn, 2013).
380
381   In sulfate reducing bacteria, transhydrogenase NfnAB plays an important role in energy
382   metabolism (Pereira et al., 2011; Price et al., 2014). If the magnitude of hydrogen isotope
383   fractionation imparted by this transhydrogenase is large, similar to other
384   transhydrogenases, then the activity of this enzyme may play a large role in setting
385   δ^2H_{lipid}. This role may extend to the observed variations in δ^2H_{lipid} as a function of
386   substrate. In this model, NAD(P)H is produced or consumed by a variety of metabolic
387   reactions in the cell (Table S2), but cycling of NAD(P)H through NfnAB could play a
388   dominant role in determining the δ^2H of NAD(P)H. The δ^2H_{lipid} might be closely coupled
389   to the size of the pools of oxidized and reduced purine dinucleotide coenzymes, rather
390   than simply a function of changes in NAD(P)H δ^2H. This could be a function of a
391   Rayleigh distillation as NADPH is consumed. Alternatively, enzymes such as enoyl-ACP
392   reductase, which are responsible for hydride transfer during fatty acid biosynthesis may
393   be capable of utilizing either NADH and NADPH (Bergler et al., 1996), and the preferred
394   substrate may change depending on their relative pool size. The perturbation of NfnAB in
395   mutant strains would be expected to affect the relative sizes of these pools, and could
396   help explain the observed patterns in lipids.
397
398   If NfnAB is important in determining δ^2H_{lipid} in SRB, it could also be significant in other
399   anaerobes as well. NfnAB genes are widely distributed in anaerobes, particularly in
400   Deltaproteobacteria, Thermotogae, Clostridia, and methanogenic archaea (Buckel and
401   Thauer, 2013), and thus far ubiquitous in sulfate-reducing bacteria (this study, Pereira et
402   al., 2011). Figure 7 shows the relationship of NfnAB sequences from a range of
403   anaerobes. Interestingly, all the sulfate reducing bacteria measure for lipid/water H-
404   isotope fractionation to-date (Campbell et al., 2009; Dawson et al., 2015; Osburn et al.,
405   2016; Sessions et al., 1999) contain some form of the NfnAB. While *nfnAB* sequences
406   tend to cluster phylogenetically, the gene tree shown in Figure 7 identifies potential
407   lateral gene transfer events among the SRB. The NfnAB genes from *Desulfobulbus*
408   *propionicus* and *Syntrophobacter fumaroxidans* are more similar to those of the
409   methanogenic archaea rather than the other SRB in the Deltaproteobacteria (including *D.*
410   *alaskensis* G20), which cluster together. Similar to *D. alaskensis* G20, *D. propionicus*

411 and *S. fumaroxidans* are SRB that are capable of fermentative growth on compounds such
412 pyruvate (both) and fumarate (*S. fumaroxidans*).
413
414 In *D. alaskensis* G20, the catalytic role of the NfnAB transhydrogenase shows a
415 relationship to the δ^2H_{lipid} patterns. During growth on pyruvate/sulfate, electrons are
416 predicted to flow from pyruvate to ferredoxin, then from ferredoxin through NfnAB to
417 produce reduced NADPH (Price et al., 2014). That study pointed out that the reaction of
418 transhydrogenase is probably required to produce sufficient NADPH for biosynthesis,
419 even though the experiments were done in the presence of yeast extract, which minimized
420 the importance of this reaction. In contrast, our isotopic experiments used a defined
421 medium lacking yeast extract, so the importance of the transhydrogenase reaction would
422 not be minimized. For both the wild type and mutant, growth on pyruvate/sulfate
423 produced lipids that uniformly had the most negative $^2\varepsilon_{total}$ across all our experiments.
424 This experiment showed no phenotype for the *nfn* mutants, either in isotopic composition
425 or in growth rate.
426
427 Sulfate reduction using malate likely employs NfnAB-2 to produce NADPH by oxidizing
428 NADH and reduced ferredoxin (Price et al., 2014). Fumarate respiration operates in a
429 manner similar to malate. These two substrates can be interconverted by fumarase (Price
430 et al., 2014), so this similarity is likely to be related to similar growth and electron flow.
431 Growth on each of these substrates produces similar patterns in hydrogen isotope
432 fractionation. In each case, the wild type strain produces lipids with $^2\varepsilon_{total}$ near -140‰,
433 which is not as depleted in deuterium as lipids produced during growth on pyruvate. In
434 contrast to growth on pyruvate, the mutant strains produce substantially less depleted
435 lipids, resulting in a lesser degree of fractionation ($^2\varepsilon_{total}$) than the wild type. One
436 explanation for this difference is that the mutation of one paralog of NfnAB in this strain
437 changed the ratio of reduced to oxidized dinucleotides in the cell, with a higher ratio of
438 NADPH to $NADP^+$ and a lower ratio of NADH to NAD^+. A second possibility is that the
439 change in $^2\varepsilon_{total}$ is a consequence of the growth defect of the mutant strains.
440
441 Previous work has investigated the relationship of growth rate to $^2\varepsilon_{total}$. Zhang et al.
442 (2009) did not observe a systematic relationship in the aerobic organisms that they
443 studied. However, a negative relationship was observed between growth rate and the
444 water-alkenone hydrogen isotope fractionation in the coccolithophores *Emiliania huxleyi*
445 and *Gephyrocapsa oceanica* (Schouten et al., 2006). This observation is similar to that
446 reported here, although the slope is steeper for *D. alaskensis* G20. Microbial lipids were
447 recently reported to change their δ^2H_{lipid} with growth phase (Heinzelmann et al., 2015),
448 although this effect was relatively minor. Algal lipids have been reported to modulate
449 δ^2H_{lipid} as a function of physiological state (Estep and Hoering, 1980; Romero-Viana et
450 al., 2013). Each of these relationships could be conceivably related to changes in the
451 turnover rate or ratios of intracellular metabolites, but specific metabolomics data
452 elucidating these relationships has yet to be produced.
453
454 Fermentation of pyruvate by *D. alaskensis* G20 likely involves the reduction of pyruvate
455 with NADH by malic enzyme (ME; Dde_1253) to malate (Meyer et al., 2014), which is
456 then dehydrated by fumarase to fumarate, and then reduced to succinate (*see* Price et al.

457 2014). The oxidative branch of this fermentation involves the transformation of pyruvate
458 to acetate, which reduces ferredoxin. Reduced ferredoxin is recycled via flavin-based
459 electron bifurcation, catalyzed by Hdr-Flox-1 (Meyer et al., 2014), but may also interact
460 with NfnAB in the same way as during pyruvate respiration, in an electron confurcation
461 reaction involving NADH, producing NADPH. Wild type *D. alaskensis* G20 grown by
462 pyruvate fermentation produced lipids that showed $^2\varepsilon_{total}$ comparable to that produced
463 during pyruvate respiration. However, the *nfnAB-2* mutants grown by pyruvate
464 fermentation generated an $^2\varepsilon_{total}$ slightly more enriched than the wild type (Figure 4,
465 mutants: -160‰ and -162‰, relative to WT: -168‰). If the *nfnAB-2* mutation inhibited
466 NADPH formation, this pattern is opposite of that seen in other experiments, because it
467 results in a less fractionation (a less negative $^2\varepsilon_{total}$) at a lower predicted NADPH/NADP
468 ratio. Nonetheless, the shift is minimal (<10‰) and the important reactions in ferredoxin
469 recycling may be complicating this interpretation. Unlike the result in Meyer et al.
470 (2014), *nfnAB-2* mutants in our experiments did not show a growth defect on pyruvate
471 fermentation. This may in part be related to partial pressures of H_2 produced by growing
472 strains (not monitored herein). Alternatively, this may be due to the presence of the
473 second transhydrogenase in G20, *nfnAB-1*, as highlighted above with respect to the
474 pyruvate/sulfate experiments.
475
476 Fumarate fermentation in sulfate reducing bacteria is not well studied, but it is likely a
477 complex metabolism. Wild type *D. alaskensis* G20 has nearly identical growth rates
478 during fumarate fermentation and respiration. The *nfn* mutants grow more slowly than the
479 wild type, but show little difference between fumarate fermentation and respiration.
480 Respiration and fermentation of fumarate, along with respiration of malate, show nearly
481 identical patterns in growth rate and in $^2\varepsilon_{total}$ for each of our three strains (Figure 4). This
482 suggests an underlying mechanism uniting these growth conditions.
483
484 Fatty acid profiles across the three strains and five conditions show some correlations
485 with the total isotopic fractionation (Figure S3). The fractional abundance of branched
486 chain lipids, particularly anteiso-C17:0, is positively correlated with the fractionation and
487 negatively correlated with growth rate. We can reason two ways in which changing δ^2H
488 values of fatty acids may result in a less negative $^2\varepsilon_{total}$ (Figure S2). The isotopic ordering
489 of lipids may be altered, resulting in a net change in $^2\varepsilon_{total}$; alternatively, there could be a
490 consistent shift in the $^2\varepsilon_{lipid}$ of most or all lipids. Data shown in Figures 3 and 5 rule out
491 the first option, and show that almost all individual $^2\varepsilon_{lipid}$ change in concert between
492 conditions. This suggests that the driving mechanism for changes in $^2\varepsilon_{total}$ relates to
493 process relevant to all lipids. Processes related to the production and consumption of
494 NADPH are consistent with this role.
495
496 Integrating data from all five experimental conditions and three strains suggests a
497 relationship between growth rate and $^2\varepsilon_{total}$ (Figure 6). We do not yet have a theoretical
498 prediction for the nature of this relationship, however the relationship is consistent with a
499 linear, exponential decay, or hyperbolic relationship between growth rate and isotope
500 fractionation. This pattern is similar, although opposite in sign, to that seen in sulfur
501 isotope fractionation imposed by SRB during dissimilatory sulfate reduction (Chambers
502 et al., 1975; Kaplan and Rittenberg, 1964; Leavitt et al., 2013; Sim et al., 2011, 2013).

503 Models aimed at addressing the growth rate—fractionation relationship in sulfur isotopes
504 have focused on ratios of intracellular metabolites and redox state (Bradley et al., 2016;
505 Wing and Halevy, 2014). Similar controls could be at work in controlling hydrogen
506 isotope fractionation: ratios of $NAD(P)H/NAD(P)^+$ and intracellular redox state are
507 related and the partitioning of hydrogen between these pools could exert a direct effect on
508 δ^2H_{lipid}. However, we cannot rule out the possibility that the correlation with growth rate
509 is fortuitous, and correlations between δ^2H_{lipid} and growth rate have not been observed in
510 other studies (Dawson et al., 2015; Zhang et al., 2009). Ongoing work is aimed at testing
511 this hypothesis, through growth of SRB in chemostats. If this hypothesis holds, then $^2\varepsilon_{total}$
512 and δ^2H_{lipid} of sulfate reducers may be able to provide a critical constraint on the
513 interpretation of sulfur isotope patterns in natural systems, such as marine sediments and
514 anoxic water columns.
515
516 Transhydrogenases related to *nfnAB* are widely distributed in anaerobes (Figure 7), and
517 reactions catalyzed by this class of transhydrogenase may influence sedimentary lipid H-
518 isotopic distributions in a wide range of natural settings. The metabolic role of NfnAB
519 has been investigated in other anaerobes, notably thermophilic Clostridia (Lo et al.,
520 2015), and similar studies of hydrogen isotope fractionation using these strains may
521 indicate whether the patterns uncovered here in sulfate reducers are more generally
522 applicable throughout obligate anaerobes, and the microbial domains of life in general.
523
524 The biggest differences in δ^2H that we observe in these experiments are not between
525 growth on various substrates or between wild type and mutant, but among individual fatty
526 acids grown in a single culture. Understanding the biosynthetic mechanisms that are
527 driving these differences will be key to the interpretations of the isotopic compositions of
528 sedimentary fatty acids. The isotopic ordering is consistent, and differences in $^2\varepsilon_{total}$ are
529 not driven by changing abundances of lipids with extreme δ^2H_{lipid}, but by systematic
530 changes across all lipids (Figure 5, S2).
531
532 The enrichment in δ^2H_{lipid} of saturated fatty acids relative to their unsaturated
533 homologues may be tied to biosynthesis. During fatty acid elongation, double bonds are
534 introduced during each successive two-carbon addition. These *trans* double bonds are
535 reduced by enoyl-ACP reductase, FabI (Kass and Bloch, 1967). A *trans* to *cis*
536 configurational change can be introduced to the 10-carbon intermediate, preventing the
537 function of FabI and conserving the double bond during further chain elongation. Fatty
538 acids that have undergone this conversion are depleted in δ^2H_{lipid}, suggesting that the
539 hydrogen transferred by FabI during fatty acid elongation is enriched in δ^2H relative to
540 average δ^2H_{lipid}. However, we cannot rule out the possibility that saturated and
541 unsaturated fatty acids were produced at different times in the growth of our cultures and
542 that the isotopic differences may reflect a different process than that articulated here.
543
544 Another observation necessitating explanation is the depletion in δ^2H_{lipid} of anteiso-
545 branched fatty acids relative to the straight chain fatty acids (Figure S2). Biosynthesis
546 offers a potential explanation here as well. Straight-chain fatty acids are extended two
547 carbons at a time by successive transfers of acetyl units (transferred as malonyl-ACP with
548 the loss of CO_2 during each transfer; ACP = acyl carrier protein). The primer for this
549 chain extension is acetyl-CoA in the case of straight chain fatty acids, but differs for iso-

550 and anteiso- branched fatty acids (Kaneda, 1991). Even-numbered iso- branched fatty
551 acids use isobutyryl-CoA (derived from valine) as a primer, while odd-numbered iso-
552 branched fatty acids use isovaleryl-CoA (derived from leucine). Even-numbered anteiso-
553 branched fatty acids use 2-methylbutyryl-CoA (derived from isoleucine) as a primer
554 (Kaneda, 1991). One possible explanation for a δ^2H-depletion in anteiso- branched fatty
555 acids is a depletion in the δ^2H content of isoleucine. Compound-specific analysis of δ^2H
556 of amino acids has only recently been developed, but initial results suggest large
557 differences in the δ^2H content of various amino acids (Fogel et al., 2015). This new
558 analytical technique could prove powerful in understanding the diversity of δ^2H$_{lipid}$ values
559 produced by individual organisms.
560
561
562 **5.   Conclusions**
563
564 The magnitude of hydrogen isotope fractionation in *D. alaskensis* G20 is influenced by
565 the growth substrate, with growth on pyruvate exhibiting a different isotopic phenotype
566 than growth on other substrates. Large differences are observed in the δ^2H$_{lipid}$ among
567 individual lipids under all conditions. These differences may relate to biosynthesis, but
568 are not fully accounted for. Wild type and *nfnAB-2* mutants show large differences in
569 $^2\varepsilon_{total}$ under conditions in which NfnAB-2 is predicted to play a significant role in energy
570 conservation. This phenotype was observed across the entirety of the *D. alaskensis* G20
571 fatty acid profile. While $^2\varepsilon_{total}$ correlates with modest changes in the fatty acids produced,
572 it cannot be accounted for by changes in the abundance of individual lipids. These
573 changes in apparent fractionation indicate a role for NfnAB-2 in determining both growth
574 rate and δ^2H$_{lipid}$ for *D. alaskensis* G20, particularly when grown on malate or fumarate.
575 NfnAB is widely distributed in anaerobes, and may play a role in determining δ^2H$_{lipid}$ in
576 other organisms. Future work will aim to isolate these variables and further strengthen
577 our understanding of the roles of growth and metabolic rate, substrate-induced
578 differences in energy conservation pathways, and expression of transhydrogenase as key
579 factors in the determining the hydrogen isotope ratios of lipids.
580
581 **6.   Acknowledgements**
582

597 **7.   References**

598

599 Bergler, H., Fuchsbichler, S., Högenauer, G., and Turnowsky, F. (1996). The enoyl-[acyl-
600   carrier-protein] reductase (FabI) of Escherichia coli, which catalyzes a key
601   regulatory step in fatty acid biosynthesis, accepts NADH and NADPH as cofactors
602   and is inhibited by palmitoyl-CoA. *Eur. J. Biochem.* 242, 689–694.
603 Bizouarn, T., Grimley, R. L., Cotton, N. P. J., Stilwell, S. N., Hutton, M., and Jackson, J.
604   B. (1995). The involvement of NADP(H) binding and release in energy transduction
605   by proton-translocating nicotinamide nucleotide transhydrogenase from Escherichia
606   coli. *BBA - Bioenerg.* 1229, 49–58.
607 Bradley, A. S., Leavitt, W. D., Schmidt, M., Knoll, A. H., Girguis, P. R., and Johnston,
608   D. T. (2016). Patterns of sulfur isotope fractionation during Microbial Sulfate
609   Reduction. *Geobiology* 14, 91–101.
610 Buckel, W., and Thauer, R. K. (2013). Energy conservation via electron bifurcating
611   ferredoxin reduction and proton/Na+ translocating ferredoxin oxidation. *Biochim.*
612   *Biophys. Acta - Bioenerg.* 1827, 94–113.
613 Campbell, B. J., Li, C., Sessions, A. L., and Valentine, D. L. (2009). Hydrogen isotopic
614   fractionation in lipid biosynthesis by H2-consuming Desulfobacterium
615   autotrophicum. *Geochim. Cosmochim. Acta* 73, 2744–2757.
616 Chambers, L. A., Trudinger, P. A., Smith, J. W., and Burns, M. S. (1975). Fractionation
617   of sulfur isotopes by continuous cultures of Desulfovibrio desulfuricans. *Can. J.*
618   *Microbiol.* 21, 1602–1607.
619 Dawson, K. S., Osburn, M. R., Sessions, A. L., and Orphan, V. J. (2015). Metabolic
620   associations with archaea drive shifts in hydrogen isotope fractionation in sulfate-
621   reducing bacterial lipids in cocultures and methane seeps. *Geobiology*, n/a–n/a.
622 Dickschat, J. S., Bruns, H., and Riclea, R. (2011). Novel fatty acid methyl esters from the
623   actinomycete Micromonospora aurantiaca. *Beilstein J. Org. Chem.* 7, 1697–1712.
624 Edgar, R. C. (2004). MUSCLE: Multiple sequence alignment with high accuracy and
625   high throughput. *Nucleic Acids Res.* 32, 1792–1797.
626 Estep, M. F., and Hoering, T. C. (1980). Biogeochemistry of the stable hydrogen
627   isotopes. *Geochim. Cosmochim. Acta* 44, 1197–1206.
628 Fogel, M. L., Newsome, S. D., Griffin, P., Bradley, C. J., and Graves, G. R. (2015).
629   Hydrogen Isotopes in Amino Acids: More than just precipitation tracers. in *27th*
630   *International Meeting on Organic Geochemistry*, 60.
631 Hayes, J. M. (2001). "Fractionation of the isotopes of carbon and hydrogen in
632   biosynthetic processes," in *Stable Isotope Geochemistry, Reviews in Mineralogy and*
633   *Geochemistry*, 225–278.
634 Heinzelmann, S. M., Villanueva, L., Sinke-Schoen, D., Sinninghe Damsté, J. S.,
635   Schouten, S., and van der Meer, M. T. J. (2015). Impact of metabolism and growth
636   phase on the hydrogen isotopic composition of microbial fatty acids. *Front.*
637   *Microbiol.* 6, 1–11.
638 Jackson, J. B. (2003). Proton translocation by transhydrogenase. *FEBS Lett.* 545, 18–24.
639 Jackson, J. B., Peake, S. J., and White, S. A. (1999). Structure and mechanism of proton-
640   translocating transhydrogenase. *FEBS Lett.* 464, 1–8.
641 Kaneda, T. (1991). Iso- and Anteiso-Fatty Acids in Bacteria : Biosynthesis , Function ,
642   and Taxonomic Significancet. *Microbiol. Rev.* 55, 288–302.

643   Kaplan, I. R., and Rittenberg, S. C. (1964). Microbiological Fractionation of Sulphur
644   Isotopes. *J. Gen. Microbiol.* 34, 195–212.
645   Kass, L. R., and Bloch, K. (1967). On the enzymatic synthesis of unsaturated fatty acids
646   in Escherichia coli. *Proc. Natl. Acad. Sci.* 58, 1168–1173.
647   Kawai, S., and Murata, K. (2008). Structure and function of NAD kinase and NADP
648   phosphatase: key enzymes that regulate the intracellular balance of NAD(H) and
649   NADP(H). *Biosci. Biotechnol. Biochem.* 72, 919–930.
650   Kuehl, J. V, Price, M. N., and Ray, J. (2014). Functional Genomics with a
651   Comprehensive Library of Transposon.
652   Larsson, A. (2014). AliView: A fast and lightweight alignment viewer and editor for
653   large datasets. *Bioinformatics* 30, 3276–3278.
654   Leavitt, W. D., Halevy, I., Bradley, A. S., and Johnston, D. T. (2013). Influence of sulfate
655   reduction rates on the Phanerozoic sulfur isotope record. *Proc. Natl. Acad. Sci. U. S.
656   A.* 110, 11244–9.
657   Letunic, I., and Bork, P. (2011). Interactive Tree of Life v2: Online annotation and
658   display of phylogenetic trees made easy. *Nucleic Acids Res.* 39, 475–478.
659   Lo, J., Zheng, T., Olson, D. G., Ruppertsberger, N., Tripathi, S. a., Guss, A. M., et al.
660   (2015). Deletion of *nfnAB* in *Thermoanaerobacterium saccharolyticum* and its effect
661   on metabolism. *J. Bacteriol.* 197, JB.00347–15.
662   Markowitz, V. M., Chen, I. M. A., Palaniappan, K., Chu, K., Szeto, E., Grechkin, Y., et
663   al. (2012). IMG: The integrated microbial genomes database and comparative
664   analysis system. *Nucleic Acids Res.* 40, 115–122.
665   Marti-Renom, M. A., Stuart, A. C., Fiser, A., Sánchez, R., Melo, F., and Sali, A. (2000).
666   Comparative protein structure modeling of genes and genomes. *Annu Rev Biophys
667   Biomol Struct* 29, 291–325.
668   Meyer, B., Kuehl, J. V., Price, M. N., Ray, J., Deutschbauer, A. M., Arkin, A. P., et al.
669   (2014). The energy-conserving electron transfer system used by Desulfovibrio
670   alaskensis strain G20 during pyruvate fermentation involves reduction of
671   endogenously formed fumarate and cytoplasmic and membrane-bound complexes,
672   Hdr-Flox and Rnf. *Environ. Microbiol.* 16, 3463–3486.
673   Nichols, P. D., Guckert, J. B., and White, D. C. (1986). Determination of monosaturated
674   fatty acid double-bond position and geometry for microbial monocultures and
675   complex consortia by capillary GC-MS of their dimethyl disulphide adducts. *J.
676   Microbiol. Methods* 5, 49–55.
677   Osburn, M. R. (2013). Isotopic proxies for microbial and environmental change: insights
678   from hydrogen isotopes and the Ediacaran Khufai Formation.
679   Osburn, M. R., Dawson, K. S., Fogel, M. L., and Sessions, A. L. (2016). Fractionation of
680   hydrogen isotopes by anaerobic bacteria. *Front. Microbiol.*, in press.
681   Overbeek, R., Olson, R., Pusch, G. D., Olsen, G. J., Davis, J. J., Disz, T., et al. (2014).
682   The SEED and the Rapid Annotation of microbial genomes using Subsystems
683   Technology (RAST). *Nucleic Acids Res.* 42, 1–9.
684   Pearson, A. (2014). "Lipidomics for Geochemistry," in *Treatise on Geochemistry:
685   Second Edition*, eds. H. D. Holland and K. K. Turekian (Oxford, United Kingdom:
686   Elsevier), 291–336.
687   Pereira, I. A. C., Ramos, A. R., Grein, F., Marques, M. C., da Silva, S. M., and
688   Venceslau, S. S. (2011). A comparative genomic analysis of energy metabolism in

689   sulfate reducing bacteria and archaea. *Front. Microbiol.* 2, 69.

690 Polissar, P. J., and D'Andrea, W. J. (2014). Uncertainty in paleohydrologic
691   reconstructions from molecular δD values. *Geochim. Cosmochim. Acta* 129, 146–
692   156.

693 Price, M. N., Ray, J., Wetmore, K. M., Kuehl, J. V, Bauer, S., Deutschbauer, A. M., et al.
694   (2014). The genetic basis of energy conservation in the sulfate-reducing bacterium
695   Desulfovibrio alaskensis G20. *Front. Microbiol.* 5, 577.

696 Qi, H., and Coplen, T. B. (2011). Investigation of preparation techniques for δ 2 H
697   analysis of keratin materials and a proposed analytical protocol. 2209–2222.

698 Rabus, R., Hansen, T. A., and Widdel, F. (2006). "Dissimilatory sulfate- and sulfur-
699   reducing prokaryotes," in *The Prokaryotes*, eds. M. Dworkin, S. Falkow, E.
700   Rosenberg, K.-H. Schleifer, and E. Stackebrandt (New York, NY: Springer), 659–
701   768.

702 Rabus, R., Venceslau, S. S., Wöhlbrand, L., Voordouw, G., Wall, J. D., and Pereira, I. A.
703   C. (2015). *A Post-Genomic View of the Ecophysiology, Catabolism and
704   Biotechnological Relevance of Sulphate-Reducing Prokaryotes*.

705 RCoreTeam (2015). R: A language and environment for statistical computing. 3464.

706 Robins, R. J., Billault, I., Duan, J. R., Guiet, S., Pionnier, S., and Zhang, B. L. (2003).
707   Measurement of 2H distribution in natural products by quantitative 2H NMR: An
708   approach to understanding metabolism and enzyme mechanism? *Phytochem. Rev.* 2,
709   87–102.

710 Rodriguez-Ruiz, J., Belarbi, E., S, L. G., and Diego, L. (1998). Rapid simultaneous lipid
711   extraction and transesterification for fatty acid analyses. 12, 689–691.

712 Romero-Viana, L., Kienel, U., Wilkes, H., and Sachse, D. (2013). Growth-dependent
713   hydrogen isotopic fractionation of algal lipid biomarkers in hypersaline Isabel Lake
714   (Mexico). *Geochim. Cosmochim. Acta* 106, 490–500.

715 Rost, B. (1999). Twilight zone of protein sequence alignments. *Protein Eng.* 12, 85–94.

716 Saito, K., Kawaguchi, A., Okuda, S., Seyama, Y., and Yamakawa, T. (1980).
717   Incorporation of hydrogen atoms from deuterated water and stereospecifically
718   deuterium-labeled nicotinamide nucleotides into fatty acids with the Escherichia coli
719   fatty acid synthetase system. *Biochim. Biophys. Acta* 618, 202–213.

720 Sauer, P. E., Eglinton, T. I., Hayes, J. M., Schimmelmann, A., and Sessions, A. L. (2001).
721   Compound-specific D/H ratios of lipid biomarkers from sediments as a proxy for
722   environmental and climatic conditions. *Geochim. Cosmochim. Acta* 65, 213–222.

723 Sauer, U., Canonaco, F., Heri, S., Perrenoud, A., and Fischer, E. (2004). The soluble and
724   membrane-bound transhydrogenases UdhA and PntAB have divergent functions in
725   NADPH metabolism of Escherichia coli. *J. Biol. Chem.* 279, 6613–9.

726 Schmidt, H.-L., Werner, R. A., and Eisenreich, W. (2003). Systematics of 2H patterns in
727   natural compounds and its importance for the elucidation of biosynthetic pathways.
728   *Phytochem. Rev.* 2, 61–85.

729 Schouten, S., Ossebaar, J., Schreiber, K., Kienhui, s M. V. M., Langer, G., Benthien, A.,
730   et al. (2006). The effect of temperature, salinity and growth rate on the stable
731   hydrogen isotopic composition of long chain alkenones produced by Emiliania
732   huxleyi and Gephyrocapsa oceanica. *Biogeosciences* 3, 113–119.

733 Sessions, A. L., Burgoyne, T. W., Schimmelmann, A., and Hayes, J. M. (1999).
734   Fractionation of hydrogen isotopes in lipid biosynthesis. *Org. Geochem.* 30, 1193–

735   1200.
736   Sessions, A. L., and Hayes, J. M. (2005). Calculation of hydrogen isotopic fractionations
737   in biogeochemical systems. *Geochim. Cosmochim. Acta* 69, 593–597.
738   Silvestro, D., and Michalak, I. (2012). RaxmlGUI: A graphical front-end for RAxML.
739   *Org. Divers. Evol.* 12, 335–337.
740   Sim, M. S., Bosak, T., and Ono, S. (2011). Large Sulfur Isotope Fractionation Does Not
741   Require Disproportionation. *Science (80-.).* 333, 74–77.
742   Sim, M. S., Wang, D. T., Zane, G. M., Wall, J. D., Bosak, T., and Ono, S. (2013).
743   Fractionation of sulfur isotopes by Desulfovibrio vulgaris mutants lacking
744   hydrogenases or type I tetraheme cytochrome c 3. *Front. Microbiol.* 4, 171.
745   Smith, B. N., and Epstein, S. (1970). Biogeochemistry of the stable isotopes of hydrogen
746   and carbon in salt marsh biota. *Plant Physiol.* 46, 738–742.
747   Spaans, S. K., Weusthuis, R. a, Oost, J. Van Der, and Kengen, S. W. M. (2015).
748   Microbial Physiology and Metabolism NADPH-generating systems in bacteria and
749   archaea NADPH-generating systems in bacteria and archaea. 6, 1–27.
750   Stamatakis, A. (2006). RAxML-VI-HPC: Maximum likelihood-based phylogenetic
751   analyses with thousands of taxa and mixed models. *Bioinformatics* 22, 2688–2690.
752   Taylor, J., and Parkes, R. J. (1983). The Cellular Fatty Acids of the Sulphate-reducing
753   Bacteria, Desulfobacter sp., Desulfobulbus sp. and Desulfovibrio desulfuricans. *J.
754   Gen. Microbiol.*, 3303–3309.
755   Venning, J. D., Bizouarn, T., Cotton, N. P. J., Quirk, P. G., and Jackson, J. B. (1998).
756   Stopped-flow kinetics of hydride transfer between nucleotides by recombinant
757   domains of proton-translocating transhydrogenase. *Eur. J. Biochem.* 257, 202–209.
758   Wang, S., Huang, H., Moll, J., Thauer, R. K., Al, W. E. T., and Acteriol, J. B. (2010).
759   NADP+ Reduction with Reduced Ferredoxin and NADP+ Reduction with NADH
760   Are Coupled via an Electron-Bifurcating Enzyme Complex in Clostridium kluyveri.
761   *J. Bacteriol.* 192, 5115–5123.
762   Wing, B. A., and Halevy, I. (2014). Intracellular metabolite levels shape sulfur isotope
763   fractionation during microbial sulfate respiration. *Proc. Natl. Acad. Sci.* 111, 18116–
764   18125.
765   Zhang, X., Gillespie, A. L., and Sessions, A. L. (2009). Large D/H variations in bacterial
766   lipids reflect central metabolic pathways. *Proc. Natl. Acad. Sci. U. S. A.* 106, 12580–
767   6.
768
769

770   **TABLE(s)**
771

Average growth rates		
Treatment	Strain	$\mu_{avg.} \pm 1\sigma$ (per hour)
pyruvate + sulfate	wildtype	0.154 ± 0.029
	nfnA-2	0.172 ± 0.029
	nfnB-2	0.168 ± 0.035
malate + sulfate	wildtype	0.067 ± 0.007
	nfnA-2	0.014 ± 0.006
	nfnB-2	0.015 ± 0.004
fumarate + sulfate	wildtype	0.085 ± 0.012
	nfnA-2	0.011 ± 0.002
	nfnB-2	0.007 ± 0.006
fumarate fermetation	wildtype	0.057 ± 0.007
	nfnA-2	0.010 ± 0.002
	nfnB-2	0.015 ± 0.004
pyruvate fermetation	wildtype	0.131 ± 0.007
	nfnA-2	0.120 ± 0.001
	nfnB-2	0.149 ± 0.012

772
773   **Table 1:** Interval-weighted growth rates of *D. alaskensis* G20 wild type and *nfnAB-2*
774   transhydrogenase mutants on different substrates during sulfate respiration or substrate
775   fermentation. The range in rate is larger for experiments that exhibited bi-phasic
776   (diauxic) growth patters (e.g. fumarate + sulfate), as is apparent from the growth curves
777   (Fig. 2).
778
779

FIGURE CAPTIONS

780
781
782   **Figure 1**. (A). A schematic pathway of electron flow during pyruvate respiration or
783   fermentation in WT *D. alaskensis* G20. Electrons are transferred from pyruvate through
784   ferredoxin and NADPH, and NfnAB catalyzes electron confurcation, producing NADPH.
785   Mutation of NfnAB inhibits this reaction and may result in a relative NADPH deficiency
786   (B). Electron flow during fumarate and malate respiration or fumarate fermentation.
787   Mutation of NfnAB inhibits this reaction and may result in a relative NADPH surplus.
788
789   **Figure 2.** Growth curves for *D. alaskensis* G20 wildtype and transhydrogenase mutants.
790   (A) Wildtype, (B) *nfnA-2* transposon mutant, and (C) *nfnB-2* transposon mutant, each
791   under all 5-condition sets tested (denoted in the legends). Each symbol represents the
792   average of biological duplicate 50mL cultures. Error bars are smaller than the symbols in
793   all cases. Samples for lipid and isotopic analysis were extracted after the final time-point
794   indicated on this plot, all in early stationary phase.
795
796   **Figure 3.** The relative abundance of each fatty acid (% of total) from each strain under
797   the five different growth condition tested (A to E). Sample key: wild type (black circles,
798   dotted lines) or *nfnAB-2* transhydrogenase insertion-deletion mutants, *nfnA-2* (blue
799   diamonds, dashed lines) and *nfnB-2* (red squares, dash-dotted lines). The double bond
800   in *n*-C16, *iso*-C16, *iso*-C17, *anteiso*-C17 is located at the Δ9 carbon, and on the *n*-C18
801   and *iso*-C18 at the Δ11 carbon. The two C17:1's were in too low abundance following
802   the DMDS reaction to determine bond positions. Each symbol is the average of
803   biological replicates for each strain given that condition set, and the standard error of
804   individual fatty acid quantifications is <0.5% between biological replicates (error bar
805   significantly smaller than the symbols).
806
807   **Figure 4.** Hydrogen isotope fractionation between media water (symbols) and the mass-
808   weighted lipid pool ($^2\varepsilon_{total}$) for each treatment (horizontal bars). Vertical bars are standard
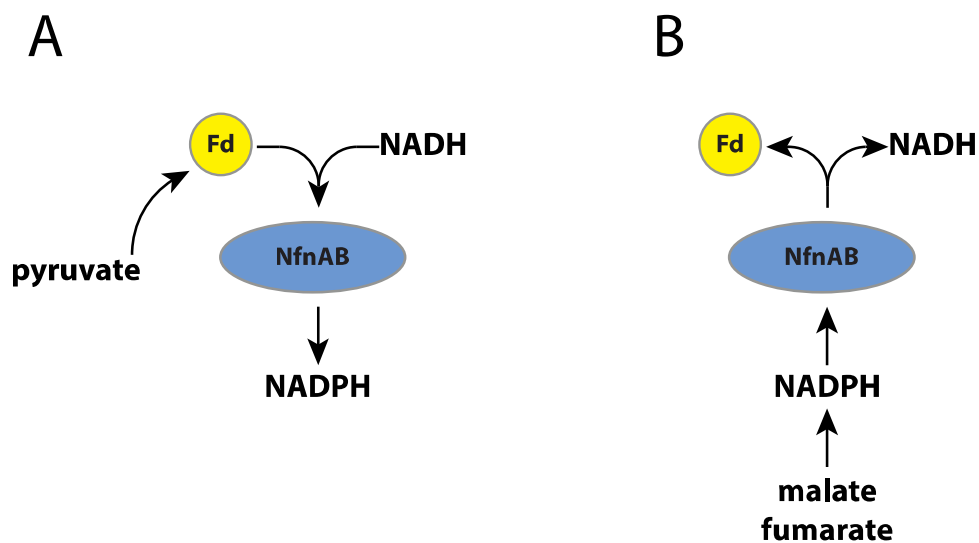809   errors on the mean (SEM).
810
811   **Figure 5.** Hydrogen isotope values for individual fatty acids relative to the medium water
812   (symbols) and the mass-weighted lipid pool ($^2\varepsilon_{total}$) for each treatment (horizontal black
813   bars). Each symbol represents the mean of biological replicates (N = 2, and technical
814   replication $n_{avg.}$ = 3, range 1 to 6), with SEM.
815
816   **Figure 6.** Average weighted growth rate (μ) versus the $^2\varepsilon_{total}$ for all experiments.
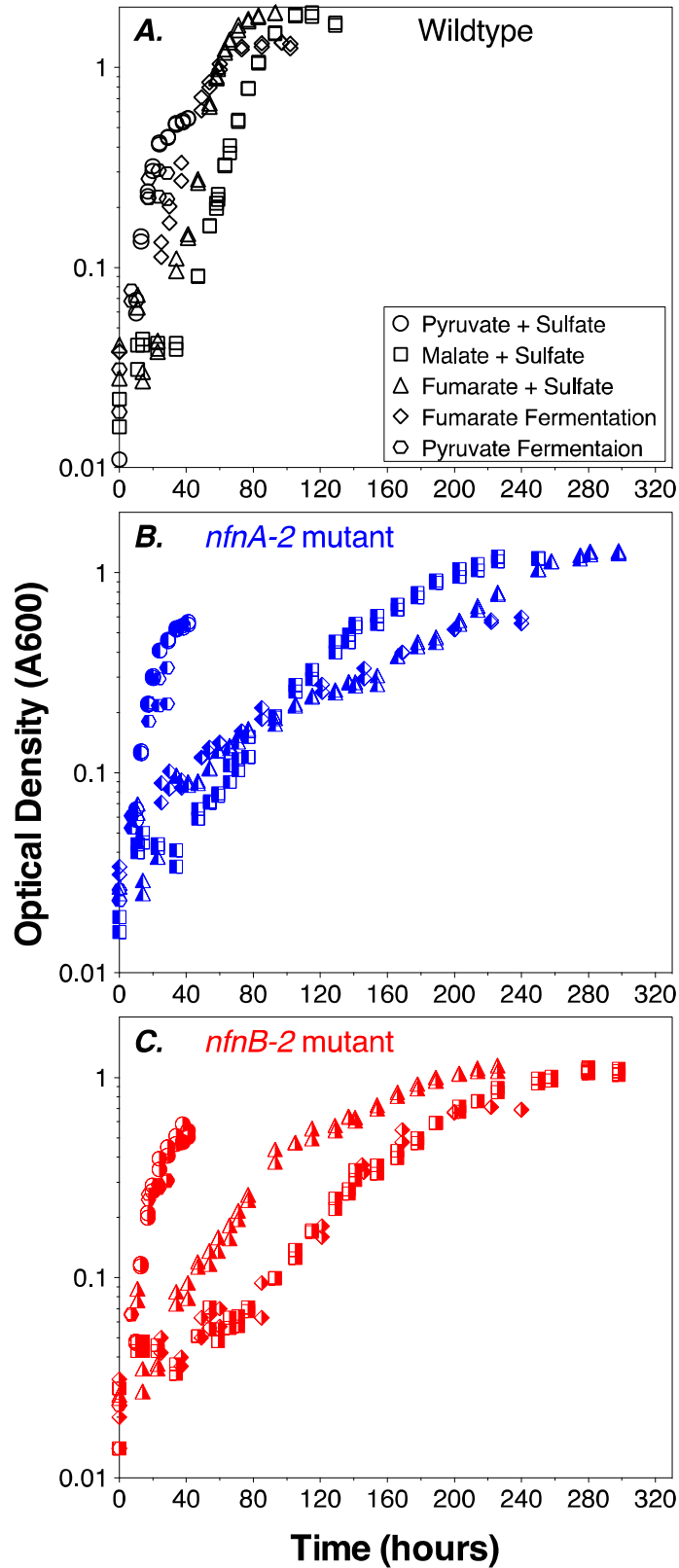817
818   **Figure 7.** Maximum likelihood phylogenetic tree of NfnAB using amino acid sequences
819   taken from the sequenced genomes of known anaerobes. Each branch is colored by
820   Phylum. Bootstrap values (out of 100) are shown at each branch point.
821
822

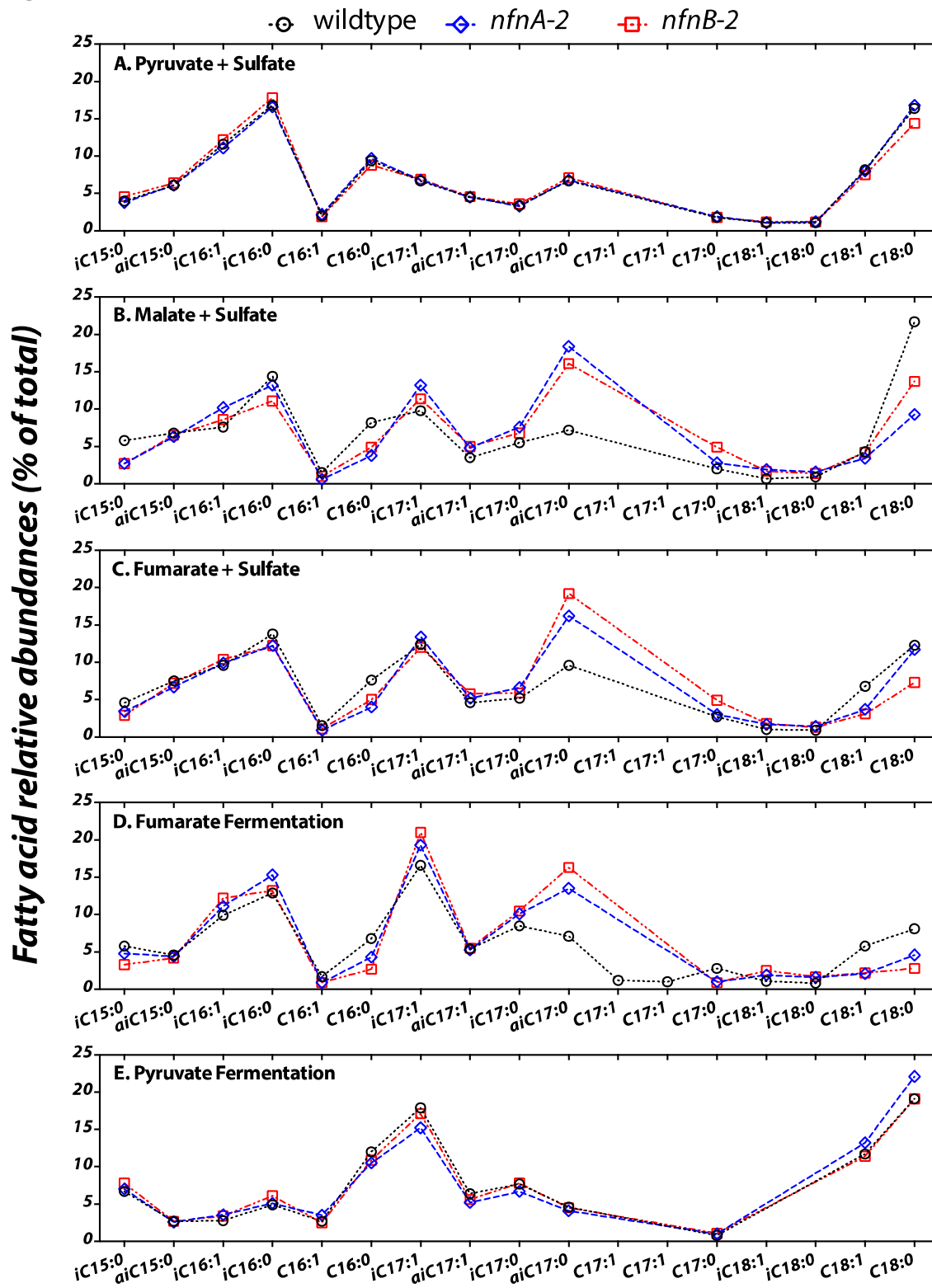823   **Figures.**
824
825   **Figure 1.**
826

A

B

827
828

829   **Figure 2.**

831   **Figure 3.**

832
833

834 **Figure 4.**

835
836

837   **Figure 5.**

838
839
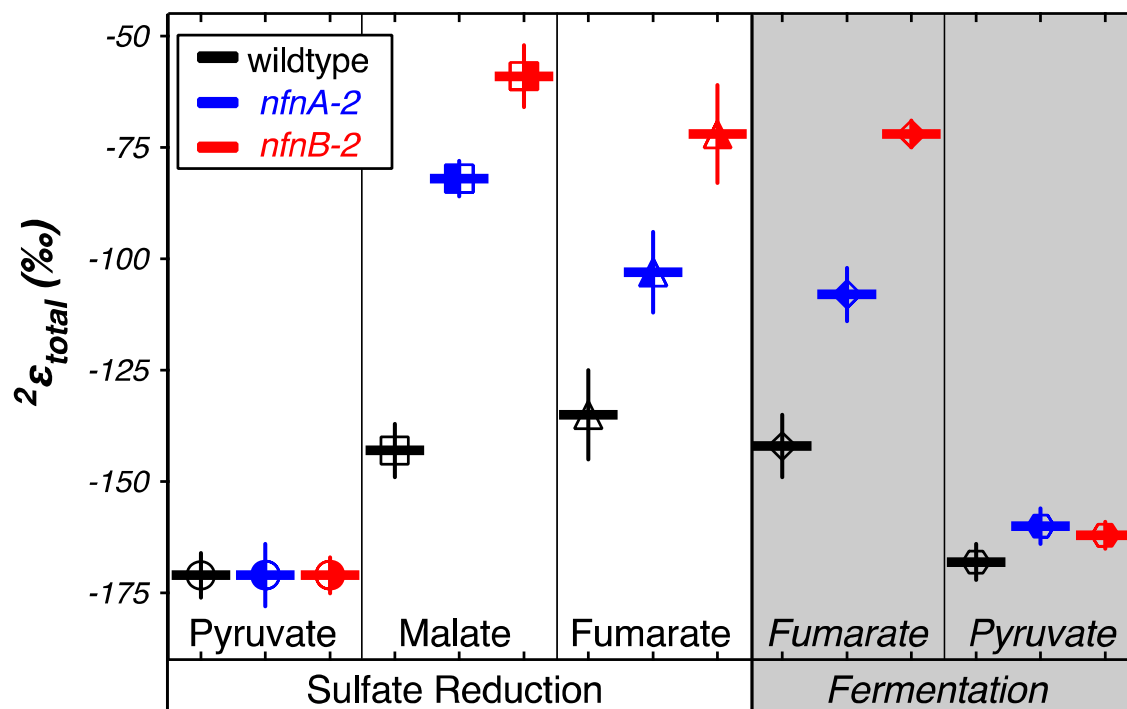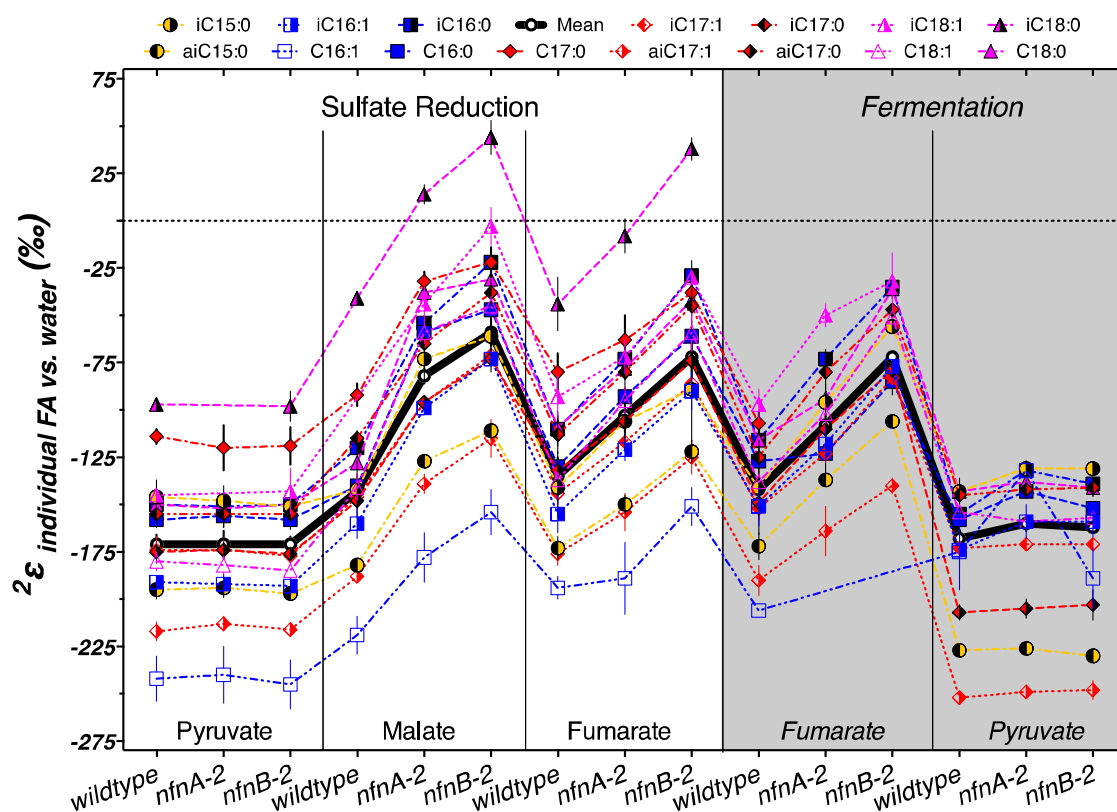
840   **Figure 6.**

841
842

843   **Figure 7.**

844
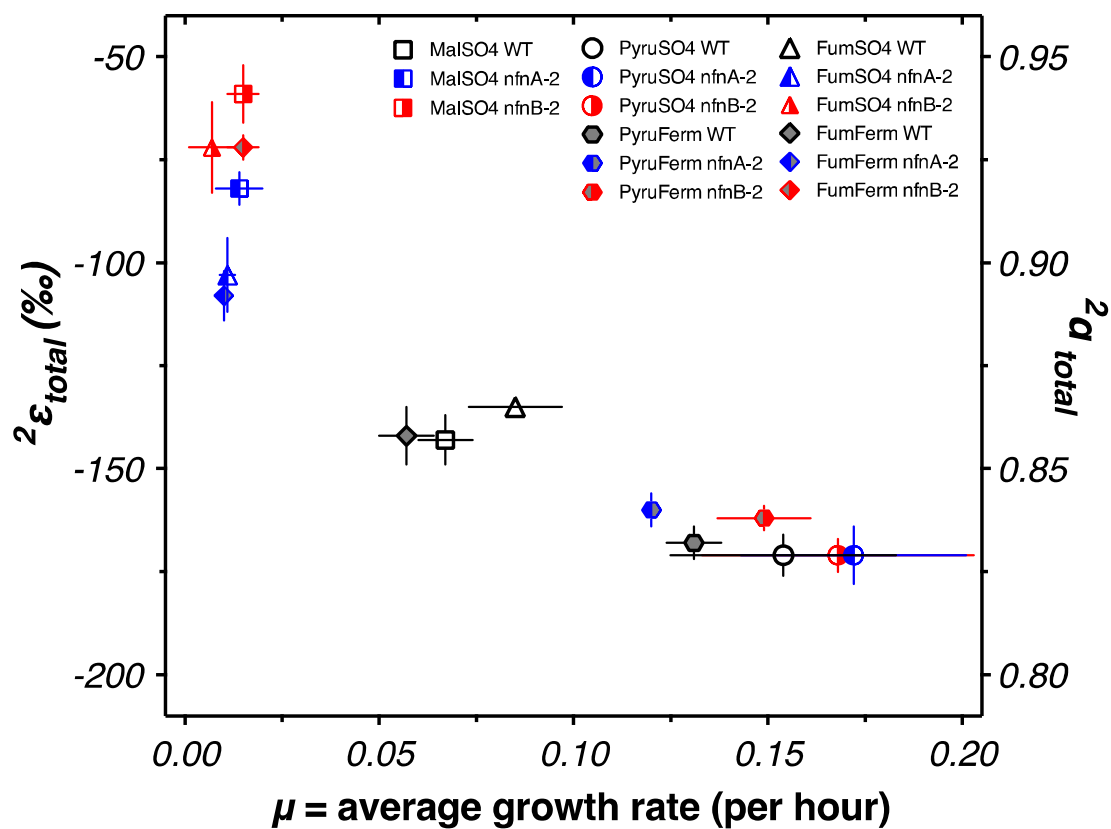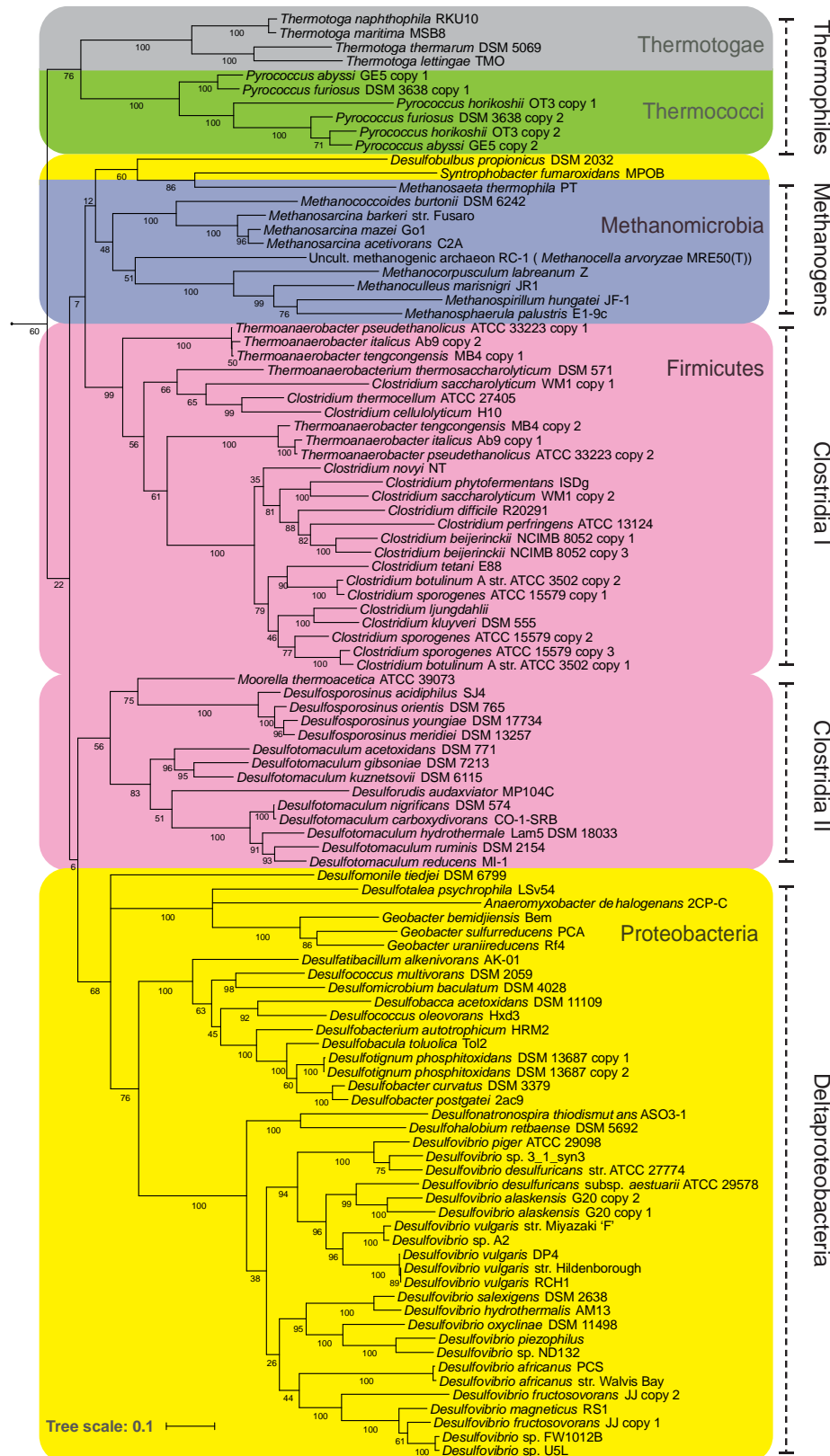
845
846   **Supplemental Figures**
847
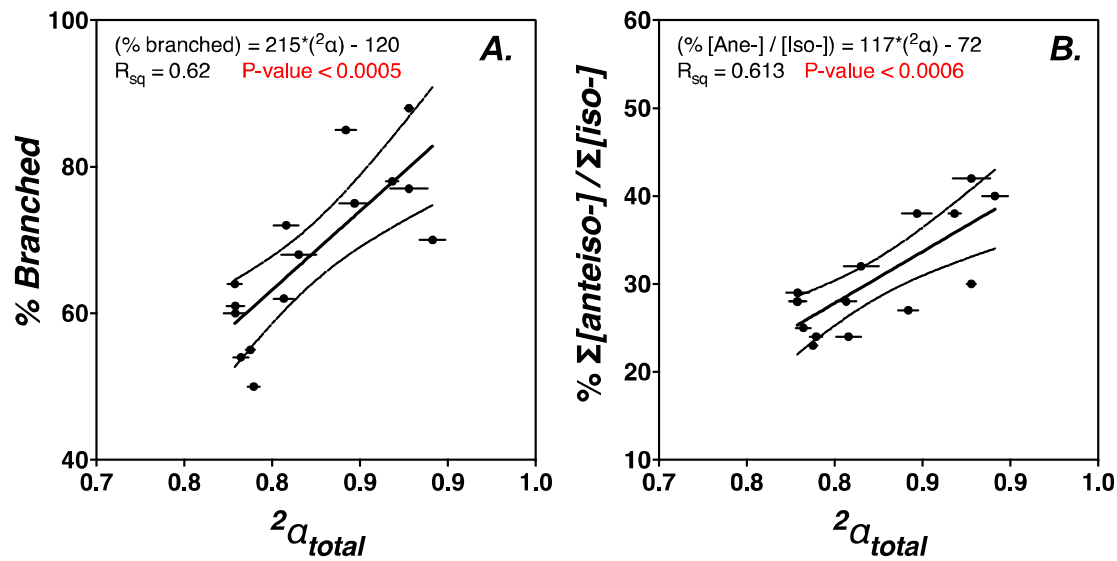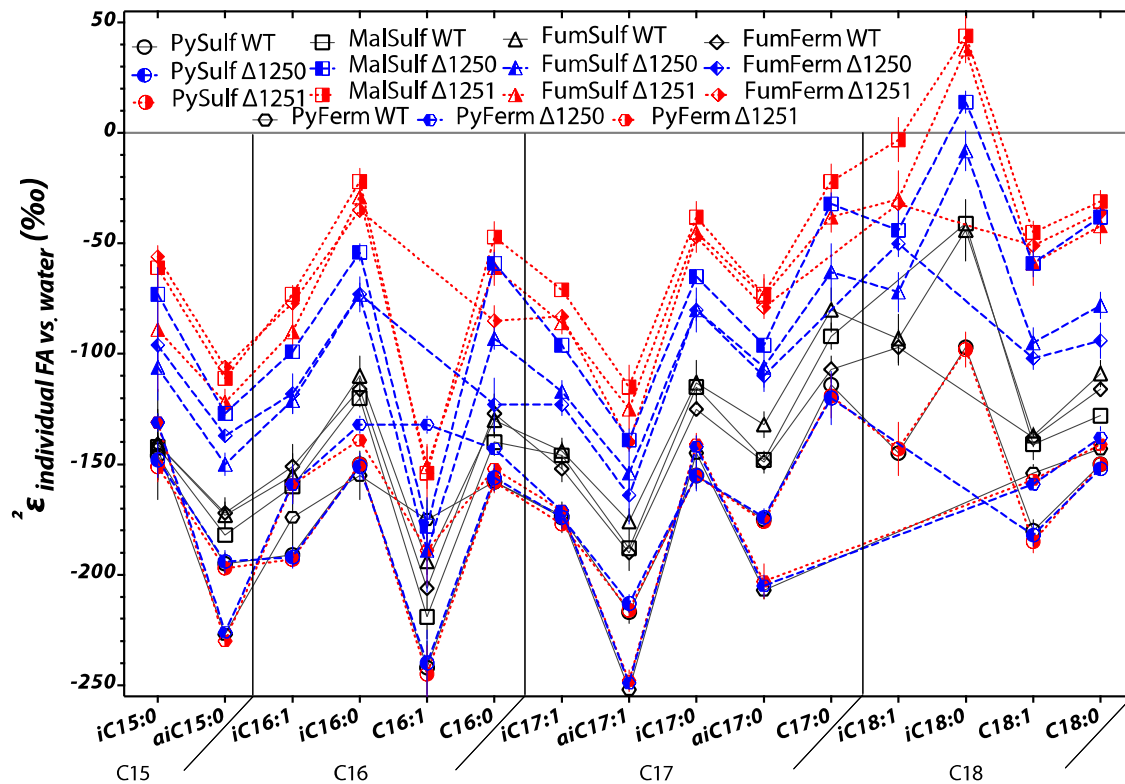848   **Figure S1.**

849
850   **Figure S1.** The mass-weighted fractionation between lipids and water versus the
851   proportion of (A) branched fatty acids, (B) the ratio of anteiso- to iso- branched fatty
852   acids.
853

854   **Figure S2.**

855
856   **Figure S2.** Hydrogen isotope values for individual fatty acids relative to medium water.
857   These are the same values as in Figure 5, but here plotted by compound (x-axis) and
858   legend-coded by experiment. Each symbol represents the mean of biological replicates
859   (N = 2, and technical replication $n_{avg.}$ = 3, range 1 to 6), with SEM.
860
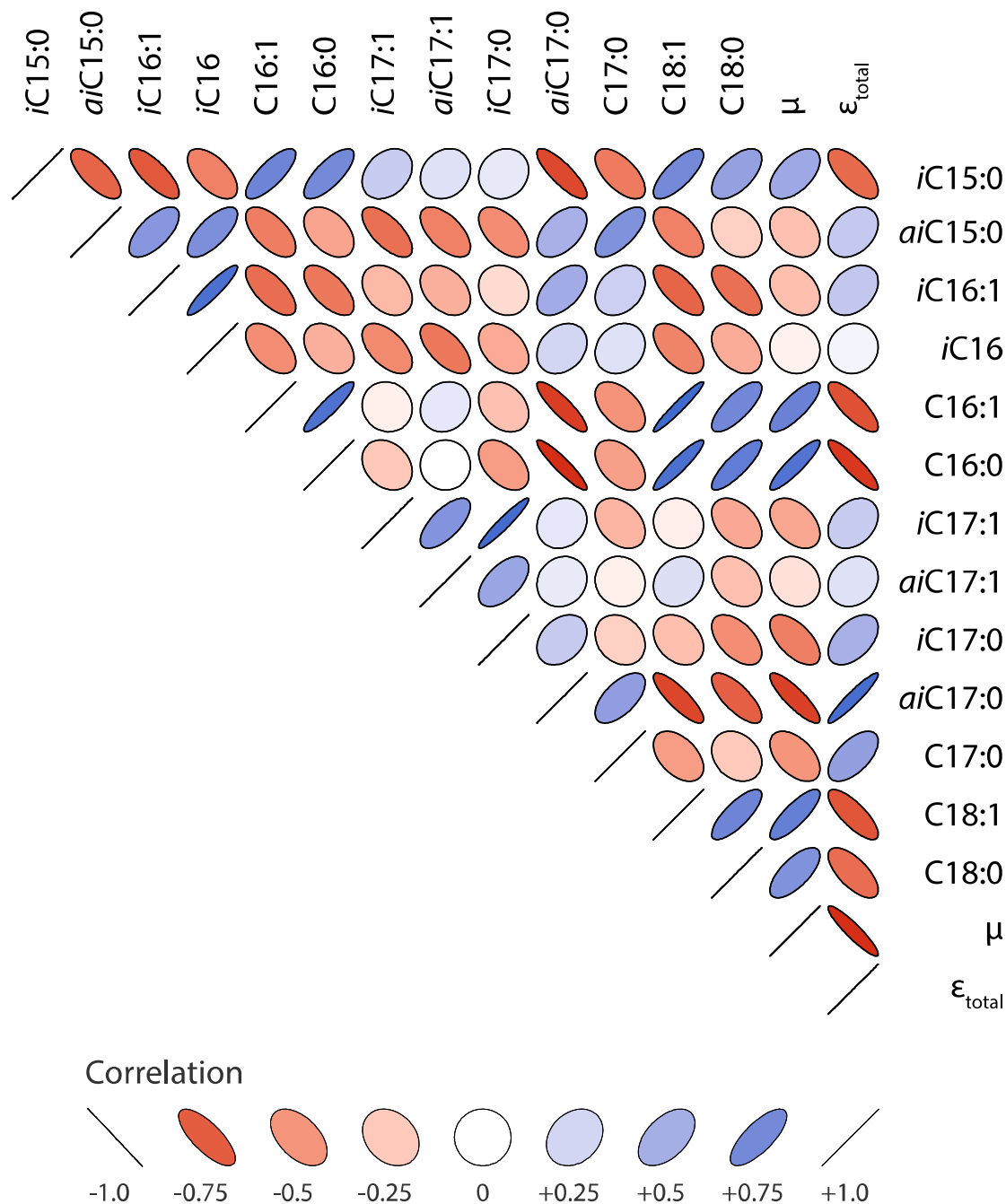
861   **Figure S3.**

862
863   **Figure S3.** Representation of Pearson correlation indices for each pair of variables.
864   Width of ellipses indicates the strength of the correlation, with narrow ellipses indicating
865   a strong correlation and circles indicating no correlation. Darker blues are stronger
866   positive correlations, darker reds are stronger negative correlations, with white indicating
867   no correlation.
868

869   **Table S1.** FAME identifications based on mass spectra and retention times

RI	shorthand	M$^+$	Free fatty acid
1687	i-C14:0	242	12-methyl tridecanoic acid
1790	i-C15:0	256	13-methyl tetradecanic acid
1798	a-C15:0	256	12-methyl tetradecanoic acid
1871	i-C16:1	268	14-methyl pentadec-9-enoic acid
1892	i-C16:0	270	14-methyl pentadecanoic acid
1905	C16:1	268	hexadec-9-enoic acid
1928	C16:0	270	hexadecanoic acid
1967	i-C17:1	282	15-methyl hexadec-9-enoic acid
1976	a-C17:1	282	14-methyl hexadec-9-enoic acid
1991	i-C17:0	284	15-methyl hexadecanoic acid
2000	a-C17:0	284	14-methyl hexadecanoic acid
2004	C17:1	282	heptadecenoic acid
2010	C17:1	282	heptadecenoic acid
2027	C17:0	284	heptadecanoic acid
2070	i-C18:1	296	16-methyl heptadec-11-enoic acid
2090	i-C18:0	298	16-methyl heptadecanoic acid
2108	C18:1	296	octadec-11-enoic acid
2132	C18:0	298	octadecanoic acid
2738	C24	382	tetracosanoic acid (standard)

870
871

872   **Table S2.** Major mechanisms of NADPH production relevant to *D. alaskensis* G20

Enzyme	EC number	G20 locus	name
G6PDH	1.1.1.49	Dde_3471	glucose-6-phosphate 1-dehydrogenase
6PGDH	1.1.1.44	Dde_3470	6-phosphogluconate dehydrogenase
IDH	1.1.1.42	Dde_3476	Isocitrate dehydrogenase
ME	1.1.1.40	Dde_1253	malic enzyme
GAPN	1.2.1.9	nd	non-phosphorylating glyceraldehyde 3-phosphate dehydrogenase
NADP+-GAPDH	1.2.1.13	Dde_2342, Dde_3736	Glyceraldehyde-3-phosphate dehydrogenase, type I
GDHs	1.1.1.47, 1.1,1,119	nd	glucose dehydrogenase
STH	1.6.1.1	nd	energy-independent soluble transhydrogenase
H+-TH	1.6.1.2	nd	energy-dependent or proton-translocating,membrane-bound transhydrogenase
FNR	1.18.1.2	Dde_3636, Dde_1251	ferredoxin-NADP reductase
SH	1.12.1.3	Dde_1212	soluble hydrogenase
NADK	2.7.1.23	Dde_2618	ATP-NAD/AcoX kinase
PDR	1.8.1.8	Dde_1301	Protein-disulfide reductase
NfnAB1	1.6.1.4	Dde_3635, Dde_3636	electron-bifurcating transhydrogenase
NfnAB2	1.6.1.4	Dde_1250, Dde1251	electron-bifurcating transhydrogenase

*most of these reactions are derived from Table 1 in Spaans et al., 2015

873